

Alongshore variability in wave energy transfer to coastal cliffs

E.C. Vann Jones^{*}, N.J. Rosser, M.J. Brain

Department of Geography, Durham University, South Road, Durham DH1 3LE, UK

ARTICLE INFO

Article history:

Received 3 January 2018

Received in revised form 6 August 2018

Accepted 13 August 2018

Available online 16 August 2018

Keywords:

Rock coast

Coastal cliff

Foreshore

Microseismic

Cliff shaking

Wave impact

ABSTRACT

The alongshore distribution of wave energy is believed to be an important control on the spatial variability of coastal erosion. There is, however, a lack of field data quantifying the alongshore variability in wave energy on rock coasts, whereby the relative control of coastline geometry versus foreshore characteristics on wave energy delivery remains unclear. A number of studies have identified high-frequency cliff-top ground shaking to be generated by wave impacts at the cliff toe during high tides (HT). To capture the variability of wave-cliff impact energy along-coast, we installed an array of cliff-top seismometers along a 1 km stretch of coastline in North Yorkshire, UK. Our aim is to constrain how wave energy transfer to the cliff toe varies, and to examine the relative energy transfer around typical coastline features, including a bay and headlands. Whilst the greatest HT ground motion energy is recorded at a headland and the lowest at the centre of the bay (5% of that observed at the headland), we identify no systematic alongshore variation in the HT ground motion energy that can be related to coastline morphology. We also note considerable variation between features of similar form: the total HT ground motion energy at one headland is only 49% of the next headland 1 km alongshore. Between neighbouring sites within the bay, separated by only 100 m, we observe up to an order of magnitude difference in ground motion energy transfer. Our results demonstrate the importance of the foreshore in driving the variations in energy delivery that we observe. Local alterations in water depth and foreshore topography control the alongshore distribution of wave energy available to generate cliff HT ground motions. Importantly, this apparently local effect overrides the influence of macroscale coastal planform morphology, which has previously been assumed to be the dominant control. The results show that foreshore characteristics that hold influence over wave energy transfer vary significantly over short (~100 m) distances, and so we expect erosion controlled by wave impacts to vary over similar scales.

© 2018 The Authors. Published by Elsevier B.V. This is an open access article under the CC BY license (<http://creativecommons.org/licenses/by/4.0/>).

1. Introduction

The distribution of wave energy along coastlines is an important control on the spatial variability of erosion (e.g. Sallenger et al., 2002; Murray and Ashton, 2013). Understanding the interactions between coastal morphology and variable incident hydrodynamics is crucial to improving our understanding of the implications of future climate change and the potential changes in coastal erosion (e.g. Bray and Hooke, 1997; Walkden and Hall, 2005; Dickson et al., 2007; Trenhaile, 2011). The focussing of wave energy and erosion around rock coastlines is controlled by prevailing wave and current directions (Carter et al., 1990), the availability and distribution of sediment (Sunamura, 1976, 1982; Limber and Murray, 2011), coastline planform and foreshore geometry (e.g. Klein and de Menezes, 2001; Bowman et al., 2009; Hapke et al., 2009; Limber and Murray, 2011; Limber et al., 2014), coastal bathymetry (e.g. Trenhaile, 1987; Komar, 1997), and relative rock strength and the resistance to wave energy transfer (Sunamura, 1977, 1992).

Studies that examine the role of coastline geometry in determining wave energy and erosion focussing are largely based on field monitoring on softer rock coasts where both sediments and beach material play a dominant role in controlling erosion (e.g. Klein and de Menezes, 2001; Sallenger et al., 2002; Bowman et al., 2009), which is also observed in numerical modelling studies of coastal change (e.g. Limber and Murray, 2011; Limber et al., 2014). Few studies, however, have examined the alongshore variability of wave energy transfer and erosion on low-sediment, rock coasts.

Recently a number of models have examined the long-term (≥ 1000 years) evolution of rock coast planform geometry and the driving processes that control morphology (e.g. Limber and Murray, 2011; Limber et al., 2014). In general, alongshore variations in shallow water bathymetry result in nearshore refraction of waves: the convergence of waves focuses energy onto headlands, and divergence disperses energy as waves enter bays (e.g. Trenhaile, 1987; Komar, 1997). Wave energy transfer to the coastline is therefore determined by the degree to which the coastline projects seaward and is thus more exposed to incoming waves and greater energies (Carter et al., 1990; Limber et al., 2014).

^{*} Corresponding author.

E-mail address: e.c.vann-jones@durham.ac.uk (E.C. Vann Jones).

A number of field-based studies have calculated the energy available to erode rock foreshores and cliffs (e.g. Stephenson and Kirk, 2000; Trenhaile and Kanyaya, 2007), and have measured the distribution of wave energy cross-shore and the influence of foreshore characteristics (Ogawa et al., 2011, 2016; Poate et al., 2016; Stephenson et al., 2017). Such studies have not considered alongshore variability in these foreshore characteristics, the resulting wave energy dissipation and transfer to the cliff. The relative importance of planform geometry versus foreshore characteristics in determining how wave energy is distributed alongshore therefore remains unknown.

Coastal cliff-top ground motions have been observed by a number of recent studies to be generated by waves in the nearshore, the foreshore and at the cliff toe and distinct frequency bands of signals are observed (e.g. Adams et al., 2005; Young et al., 2011, 2012, 2013, 2016; Dickson and Pentney, 2012; Norman et al., 2013; Earlie et al., 2015; Vann Jones et al., 2015), which typically include long-period ground motions (<0.05 Hz/ >20 s) generated by infragravity waves on the foreshore/beach (e.g. Young et al., 2011, 2012); double frequency microseisms (0.1–0.2 Hz/5–10 s) generated by the superposition of waves either in deep water, or following reflection from the coast which have a period half of that of the ocean waves (e.g. Longuet-Higgins, 1950); single frequency microseisms, generated by shallow-water waves as they interact with the seabed (e.g. Hedlin and Orcutt, 1989; Friedrich et al., 1998), where the frequency band is determined by shallow water wave periods, typically 0.1–0.05 Hz/10–20 s, although this has been shown to vary with local wave periods (e.g. Norman et al., 2013; Young et al., 2013); high frequency cliff shaking (>1 Hz) is generated by wave impacts at the cliff toe (e.g. Vann Jones et al., 2015; Young et al., 2016) or foreshore edge (Dickson and Pentney, 2012) when tide heights allow. High frequency cliff shaking generated by wave-cliff impacts, have been found to provide a valuable proxy measurement of wave energy transfer directly to the cliff (Norman et al., 2013; Young et al., 2016), with statistically-significant relationships observed with monitored cliff erosion (Vann Jones et al., 2015). To date, cliff-top ground motion studies have largely focussed on single seismometers or on shore-normal transects of multiple seismometers (Dickson and Pentney, 2012; Young et al., 2012, 2013), yet given the sensitivity of data to nearshore wave conditions and cliff toe impacts, it is reasonable to assume that alongshore variations in wave impacts and loading will be reflected in commensurate variations in microseismic response.

The aim of this study is to constrain how wave energy transfer to the cliff toe varies alongshore, focussing in particular on the energy transfer around headland and bay morphology. We use these data to assess the relative control of coastline geometry versus foreshore characteristics on energy delivery. To achieve this, we deploy an array of cliff-top seismometers to capture the short-term alongshore variability in high-frequency cliff ground motion around a hard rock, low-sediment bay and headlands. Using high-frequency ground motions as a proxy for wave impacts, and thus energy transfer directly to the cliff toe, enables us to obtain a relative measure of wave energy delivery around the coast.

2. Study site

A 1 km stretch of coast between Staithes and Port Mulgrave on the NE Yorkshire coast, UK (Fig. 1) was selected as a site, to enable us to

explore varying degrees of planform crenulation, aspect and foreshore platform configuration. The monitored stretch of coast encompasses one bay ca. 570 m in width, and two adjacent headlands. The cliffs are

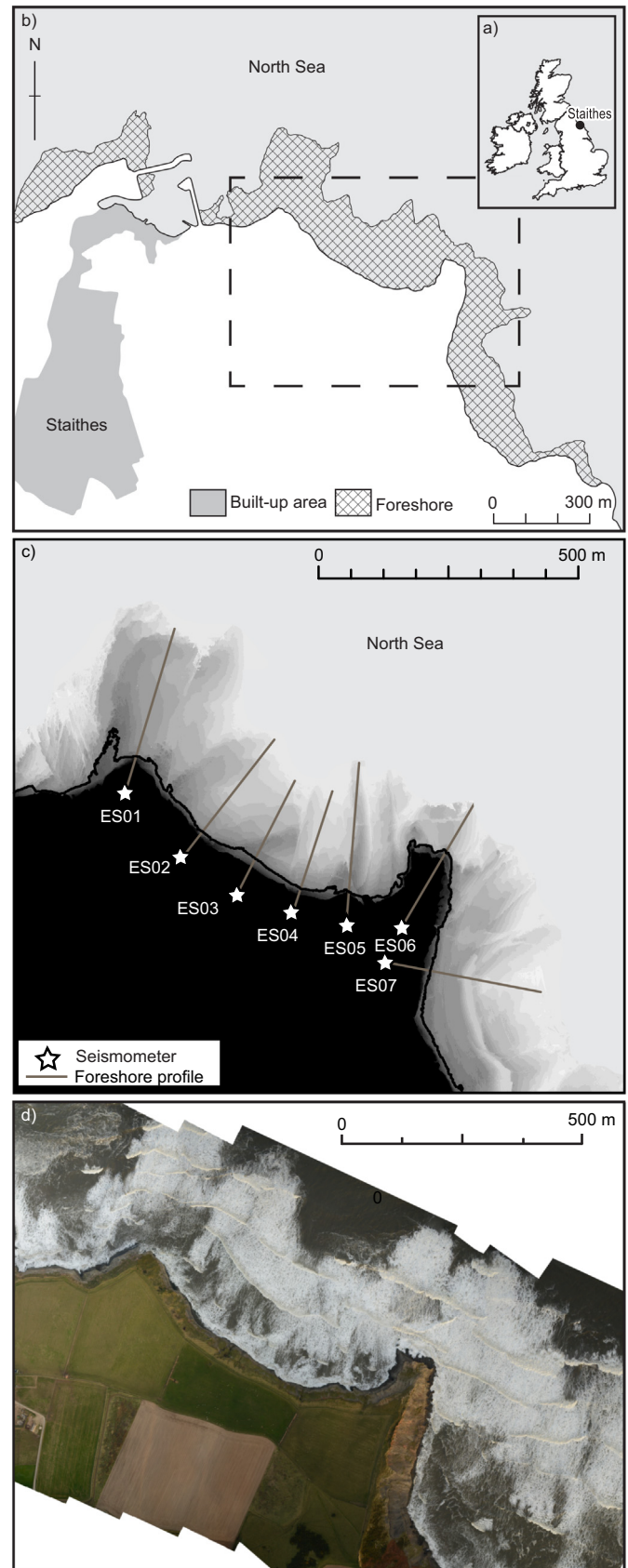


Fig. 1. Study site location. a) Location of the study site on the North Yorkshire coast, UK. b) The study site lies to the east of the village of Staithes and consists of two headlands and one bay (highlighted by the dashed box). The foreshore exposed at mean low spring tide is shown. c) DEM of the studied bay and headlands showing foreshore elevations above mean low spring tide. The locations of the seven seismometers are denoted by the stars: ES01–ES07 moving west to east. The grey lines indicate the positions of the foreshore profiles in front of each seismometer shown in Fig. 2. The black contour is at 1 m OD and elevation below this is shaded at 0.25 m intervals until the mean low spring tide elevation at -2 m OD. d) Aerial photo of the study site taken on 09/12/2017 1 h 14 min after the high spring tide. Tidal elevation at the Whitby tide gauge was 1.5 m OD, H_s recorded at the Whitby wave buoy was 4.3 m and wave direction was NNE.

45–55 m high (Fig. 2a–g), comprised of near-horizontally interbedded Lower Jurassic shales, mudstones and limestones, capped with fine-grained sandstone and glacial till, which are uniform across the study site. The site has a wide (up to 300 m) rock foreshore (Fig. 2), and a high semi-diurnal tidal range (6 m). The cliff face exposure to waves

and sea water varies considerably during the tidal cycle. During mean low spring tides the waterline can be up to 300 m from the cliff toe, but during mean high spring tides the still water level is ca. 1 m above the cliff toe. Dominant incoming wave directions are NE (Fig. 3j). Mean significant wave height (H_s) for the study period was 0.95 m

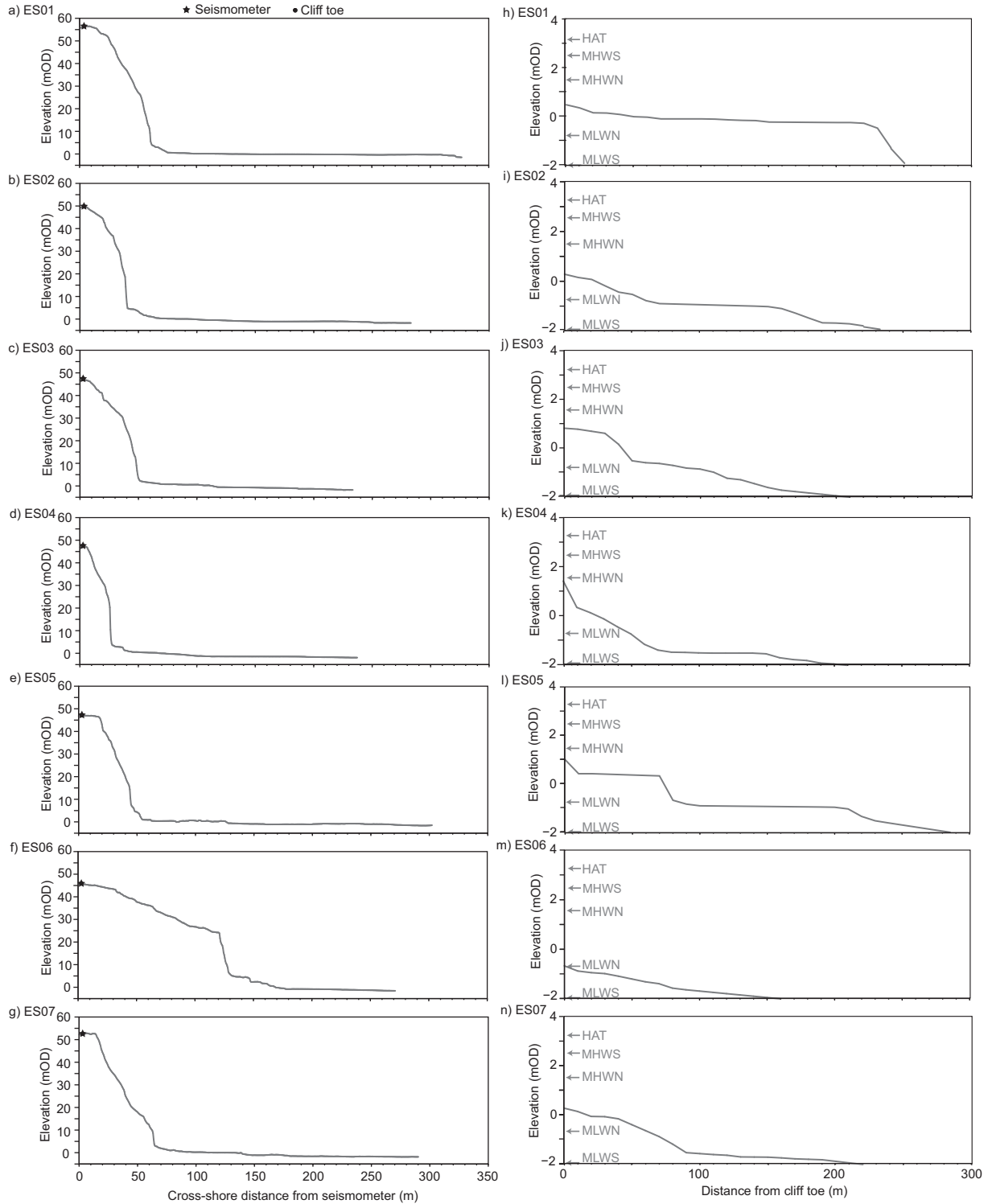


Fig. 2. Cliff and foreshore profiles at the seismometer locations: a) ES01; b) ES02; c) ES03; d) ES04; e) ES05; f) ES06; g) ES07. The stars denote the position of the seismometer at the cliff top. Detail of the foreshore profiles used within the wave model at h) ES01; i) ES02; j) ES03; k) ES04; l) ES05; m) ES06; n) ES07. Tidal elevations recorded at the Whity tide gauge are shown: highest astronomical tide (HAT), mean high water spring (MHWS), mean high water neap (MHWN), mean low water neap (MLWN), mean low water spring (MLWS). The foreshore profiles extend to the MLWS elevation.

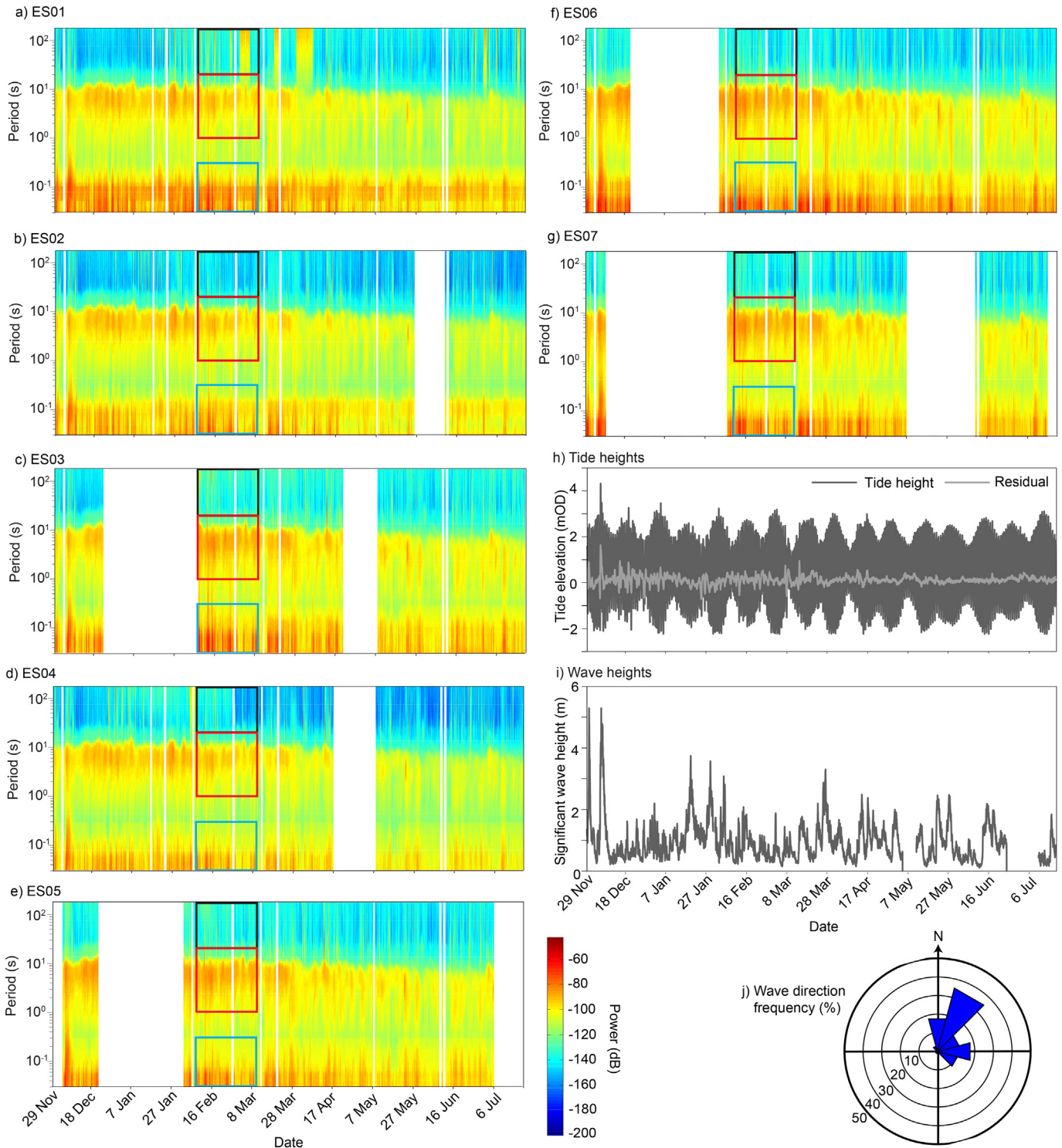


Fig. 3. Power spectrograms of cliff ground motion for the seven seismometers, tide and wave heights and wave directions for the monitoring period 29/11/2013–20/07/2014. a–g) Power spectrograms of the vertical (Z) cliff motions for the seismometers' frequency response range ($0.03-180$ s/ $33.3-0.0055$ Hz). Power is presented in decibels (dB) calculated as $10 \log_{10}((m s^{-1})^2/Hz)$. Three distinct bands of ground motions are identified in each spectrogram: long-periods (LP) (>20 s/ <0.05 Hz) (black box); microseisms (MS) ($1-20$ s/ $1-0.05$ Hz) (red box); and high frequency shaking (HT) caused by wave impacts at the cliff toe during high tides ($0.03-0.3$ s/ $33.3-333.3$ Hz) (blue box). The white zones indicate data gaps. a) ES01. b) ES02. c) ES03. d) ES04. e) ES05. f) ES06. g) ES07. h) Tide heights and residuals monitored at the Whitby tide gauge approximately 13 km south east of the field site. i) Significant wave heights (H_s) and j) wave direction frequency (%) monitored at the Whitby wave buoy, approximately 13 km south east of the study site, 1.5 km offshore and in approximately 17 m water depth. At ES01 there is a persistent band of noise at 10–20 Hz, of approximately -75 dB, the steady nature of which suggests mechanical noise. Wave and tide data are courtesy of the North East Coastal Observatory (www.northeastcoastalobservatory.org.uk).

and maximum wave height (H_{max}) was 9.26 m (both measured 1.5 km from the coastline (data courtesy of North East Coastal Observatory). The cliff morphology, foreshore topography and elevation vary

along the coast, ranging from -2 m OD at mean low spring tide level, to the highest cliff toe elevation at 1.4 m OD at the centre of the bay (Figs. 1, 2).

3. Methods

3.1. Field data

The following data were captured over an eight-month monitoring period (December 2013–July 2014):

- Seven Güralp 3TP broadband seismometers were deployed in temporary wells dug into the glacial till at the cliff-top, positioned 10 m from the cliff edge, spaced at ca. 100 m intervals along the coast (ES01–ES07, Fig. 1c). Ground motion velocities in three components (N–S, E–W, vertical (Z)) were sampled at 100 Hz. The flat frequency response of the seismometers is 120 s–50 Hz.
- At each site the foreshore profile normal to the cliff face was extracted from a high-resolution airborne LiDAR survey collected in 2015 at low tide (Fig. 1c). To extract a profile, the point cloud (ca. 60 ppm) was gridded using kriging to generate a DEM at 0.25 m resolution, from which a shore-normal profile was calculated at each instrument position (Figs. 1c, 2h–n).
- Monitored tide and wave heights (sampled every 15 min and 30 min, respectively) were obtained from a nearby tide gauge and wave buoy both at Whitby (ca. 13 km south east) (data courtesy of North East Coastal Observatory, www.northeastcoastalobservatory.org.uk). The buoy is situated 1.5 km offshore and in a water depth of approximately 17 m. Monitored wind velocities were obtained from a nearby Met Office (2006) weather station at Loftus (ca. 5 km west).

3.2. Data processing and modelling

3.2.1. Seismic data

The vertical component (Z) was used to avoid signal contamination due to ground tilt, which can adversely affect the horizontal motion recorded (e.g. Bormann, 2009; Young et al., 2012). Days containing noise due to instrument errors (e.g. loss of power), or maintenance periods, were removed. Data gaps varied between the instruments (Fig. 2a–g). Only time periods when all seven seismometers were working in parallel (95 days) were used in this analysis.

Ground motion velocity was bandpass-filtered to the frequency range 3.3–33.3 Hz, which we observed to represent cliff shaking caused by wave impacts at the cliff toe during high tides (HT) at this site. Previous studies have demonstrated that high-frequency cliff shaking, with the frequency range varying slightly between study locations, produces higher correlation coefficients with modelled and measured cliff toe wave conditions than microseism (MS) and long-period (LP) frequencies that represent wave loading in the nearshore and offshore (Norman et al., 2013; Vann Jones et al., 2015; Young et al., 2016). HT ground motion signals have also produced higher correlation coefficients with observed rockfall (Vann Jones et al., 2015).

Hourly statistics over the 95-day monitoring period describing HT ground motion energy ($(\mu\text{m s}^{-1})^2$) are presented: hourly total ($Total_h$), hourly maximum (Max_h) and total energy over the monitoring period ($Total$). The time series of HT ground motion energy was also aggregated by water elevation, derived from the modelled cliff toe water levels (see Section 3.2.2.1), to assess energy transfer as a function of water depth and inundation duration (see Section 4.3).

3.2.2. Wave data

3.2.2.1. Wave model. In the absence of monitored cliff toe wave conditions, a linear wave model based on that of Battjes and Stive (1985) (see Norman et al., 2013) was used to transform wave heights measured at the wave buoy. Wave heights were transformed by shoaling and energy dissipation via turbulence as they break in decreasing water depths (calculated from the tide gauge time-series for the monitoring period) across the nearshore and foreshore profile normal to the cliff seaward of each seismometer (Fig. 2h–n). The model accounts for

set-up and set-down as waves break but does not account for turbulence within surf bores after breaking, nor bed friction in the surf and swash zones. At each timestep, once waves had broken, wave heights for the remaining depth profile to the water's edge were set at the breaking wave height, which decreases with the water depth and therefore simulates further energy dissipation within the surf and swash zones. The model also does not account for energy dissipation due to wave refraction, reflection or diffraction. Although a 3D model would be desirable because of the complex foreshore topography, this was not possible due to a lack of high resolution bathymetry data. Time series of combined tide and modelled wave elevation at the cliff toe ($h_{elevation}$, m OD) and combined tide and modelled wave height above the cliff toe (h_{height} , m) were then calculated for each profile to derive inundation elevation, water surface height above the cliff toe, and inundation frequency at each site.

3.2.2.2. Model validation. Whilst no monitoring of cliff toe/foreshore waves was available for the seismometer monitoring period, wave pressure sensors (WPS (RBR Solo D, sampling at 2 Hz for 2048 samples every 30 min)) were installed on the foreshore for 13 days (20 Feb–4 Mar 2015) for a subsequent study. The WPS were positioned ca. 10 m from the cliff toe on the wave model profiles of ES01, ES04 and ES06 (within 10 m), and within 73 m from the profiles of ES05 and ES07. The WPS at ES01, ES04 and ES06 were used in the model validation.

There is a broadly linear relationship between the significant wave height (H_s) observed and modelled for all three sites individually (Fig. 4a–c), and for all combined (Fig. 4d). This indicates that at ES01 and ES06 the wave model overestimates wave heights (Fig. 4a, c), whereas at ES04 it underestimates height (Fig. 4b). Differences between modelled and monitored wave heights increase with height, and the fewer wave heights over 1 m at ES04 and smaller sample size may explain why the relationship at ES04 is underestimated. The coefficient of determination of the relationship at ES04 is also lower ($r^2 = 0.264$) than at ES01 ($r^2 = 0.416$) and ES06 ($r^2 = 0.343$), likely also because of the lack of larger H_s (>1 m). Differences in this relationship between sites illustrate the influence of the complex foreshore topography on the wave characteristics.

4. Results

4.1. Observed cliff-top seismic signals

Three distinct bands of marine-generated seismic signals are evident in the spectrograms for each instrument (Fig. 3): long period (LP) signals (>20 s/0.05 Hz) assumed to be generated by infragravity waves on the foreshore; microseisms (MS) (1–20 s/1–0.05 Hz) consisting of double frequency (DF) and single frequency (SF) microseisms; and high frequency shaking (0.03–0.3 s/3.33–33.33 Hz) attributed to wave impacts at the cliff toe during high tides (HT). Signal power for each band (LP, MS and HT) varies across the seven seismometers (Fig. 3). Commonly at this site we observe increases in HT signal power with corresponding increases in MS and LP signal power, indicative of stormier conditions with larger waves dissipating as they break across the foreshore and at the cliff during high tides and storm surges (Fig. 3). The highest HT signal power is observed at ES06 (Fig. 3f), with a peak of ~65 dB. ES07 (Fig. 3g) and ES01 (Fig. 3a) have similar peak signal powers, but these peaks occur less frequently than at ES06. ES04 (Fig. 3d) has significantly fewer HT peaks than observed at the other sites, and the peak signal power is lowest (~70 dB).

To determine the sources of these ground motion signals and their proximity to the seismometers, we examine the signals over a range of incident tide and wave conditions (Figs. 5, 6). During a spring tide storm (Fig. 5a–i) ($H_s = 3.15$ m, maximum wave height = 9.26 m, observed at the wave buoy) it is evident that both the LP and HT signal power is tidally modulated, whereby signal power increases and decreases with tide height (Fig. 5a–i). These signals are thus generated

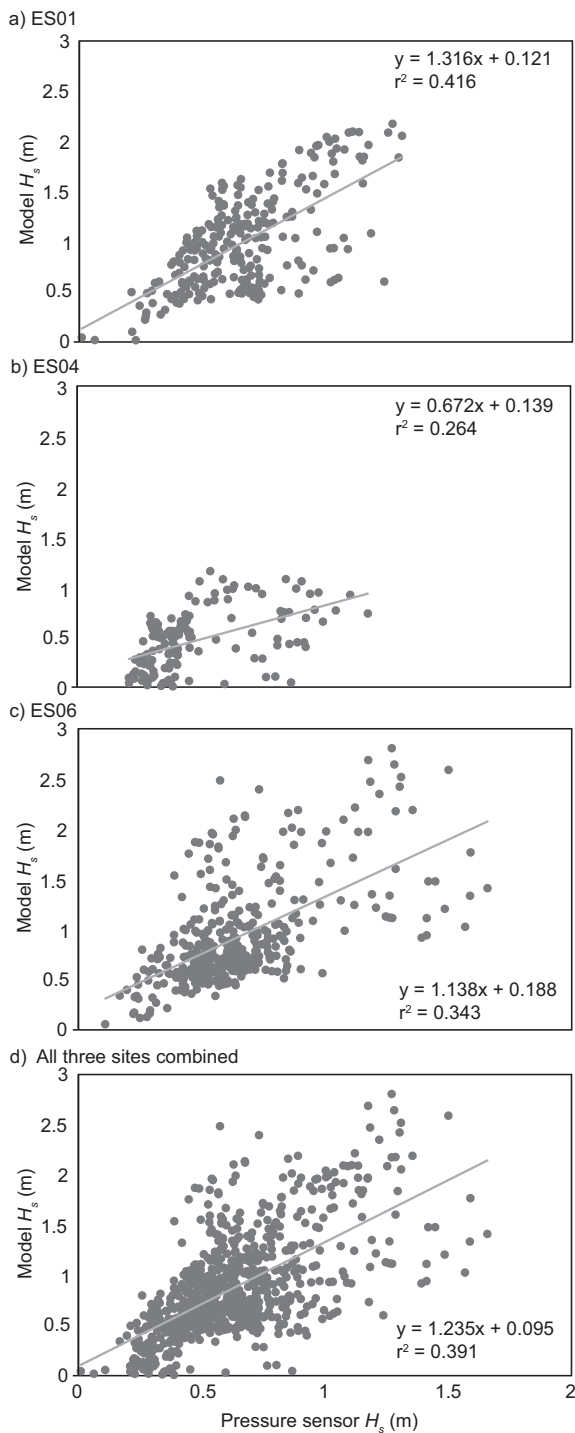


Fig. 4. Relationships between the wave pressure sensor (WPS) and the wave model significant wave heights (H_s) for a subsequent study (13-day duration, 20 Feb–4 Mar 2015) at a) ES01; b) ES04; c) ES06; and d) all three sites combined. Statistically significant relationships are presented (at p -value ≥ 0.05).

by the presence of sea on the foreshore and at the cliff. Increases in signal power in the LP signal precede those in HT (Fig. 5a–g), indicating the LP signal is generated across a wider area.

The lowest LP ground motion signal powers occur at ES07 (peak power of ~ -115 dB) (Fig. 5g), and the highest (~ -105 dB) at ES05 and ES06 (Fig. 5e, f). At ES05, ES06 and ES07, increased signal powers in the LP band also occur during low tides (Fig. 5e–g), assumed to be generated by infragravity waves on the foreshore. The duration and power of these signals represents the effectiveness of the foreshore

near these locations in either releasing infragravity energy via wave breaking, or the propagation of infragravity energy tied to swell wave groups across the foreshore.

The tidal modulation of HT can be seen clearly at all sites in the power spectrograms captured during the storm and spring tide example (Fig. 5a–i). Ground motion signal power varies across the seven instruments, with highest values (~ -60 dB) observed at the headlands, ES01 (Fig. 5a) and ES06 (Fig. 5f). During the low tides, the HT signal power is higher than during non-storm conditions (Fig. 5j–r) where it is absent, suggesting that the storm surges raise water levels up the foreshore and towards the cliff, generating wave impacts on the foreshore more proximal to the cliff toe. ES01 (Fig. 5a), ES06 (Fig. 5f) and ES07 (Fig. 5g) have higher HT signal powers during the low tides in the storm than at the other sites, which suggests that in these locations waves are able to break closer to the cliff.

The shorter duration of the peaks in HT ground motion signal powers compared to the LP signal powers corresponds to the deepest water levels at the cliff toe at each site (>2 m OD) (Fig. 5a–g), indicating HT ground motion is generated by waves impacting against the cliff face during elevated water levels. At ES06 $h_{elevation}$ (Fig. 5h) exceeds the cliff toe around 1–2 h earlier than at the other sites because it has the lowest cliff toe elevation (-0.62 m OD). ES06 thus is subject to the deepest cliff toe water depths (6.44 m OD) enabling larger waves to reach the cliff (Fig. 5h).

ES04 (Fig. 5d) has the lowest HT ground motion signal power, and a more pronounced binary distinction in the signal between high and low tides, indicating that waves only become microseismically detectable, and therefore perhaps erosively effective, during the highest tidal elevations. ES04 has the shortest duration of inundation (Fig. 5h), the highest cliff toe elevation (1.4 m OD), and as a result, the lowest peak $h_{elevation}$ (4.76 m OD) (Fig. 5h).

Higher MS signal powers occur at ES05, ES06 and ES07 during storm conditions (Fig. 5e–g) (peak power of ~ -80 dB compared to peaks of -92 dB at ES01–ES04, Fig. 5a–d). During the high tides, the MS signal powers at ES05–ES07 also extend across a wider range of periods, from 20 s to <1 s, where the MS ground motion signals merge with the HT ground motion signals (Fig. 5e–g). Differences in MS signal powers between the sites demonstrate that some of the MS signal power must be generated by gravity waves on the foreshore/in the nearshore local to each seismometer.

During less energetic spring tides ($H_s = 1.05$ m, maximum wave height = 3.5 m at the wave buoy) (Fig. 5j–r) the HT and LP ground motion signals are still evident during each high tide at all 7 sites, however the HT and LP signal power values and durations are lower and shorter compared to the storm spring tide example (Fig. 5a–g). At ES06 (Fig. 5o) the peak HT signal power is 15 dB lower and the peak LP signal power is 25 dB lower, and approximately 3 h shorter. Both the LP and HT signal powers are weakest during the second high tide (Fig. 5j–p) when peak tide elevation is 3.1 m OD (Fig. 5q) and peak H_s is 0.8 m (Fig. 5r). The wave heights are similar to those during the first tide of the storm example (Fig. 5i) when the HT and LP seismic signals are absent (Fig. 5a–g), however the higher tide elevation (Fig. 5q) enables the HT signal to be generated. It is therefore the combination of tide and wave height that are important to the generation of HT. Differences in HT signal power between sites are more apparent during less energetic conditions (Fig. 5j–p) than during the storm example (Fig. 5a–g).

During stormy neap tides ($H_s = 1.88$ m, maximum wave height = 6.09 m at the wave buoy) the HT and LP ground motion signals are only evident during high tides (peak = 1.85 m OD) when H_s is ~ 2 m (Fig. 6a–i). The signal power and duration of the LP signals is lower and shorter (for example at ES06 ~ 10 dB lower and ~ 3 h shorter, Fig. 6f) than during the spring tide storm (Fig. 5a–g), as lower tide heights and a smaller storm surge result in shorter foreshore, and cliff inundation durations. Smaller wave heights result in lower signal

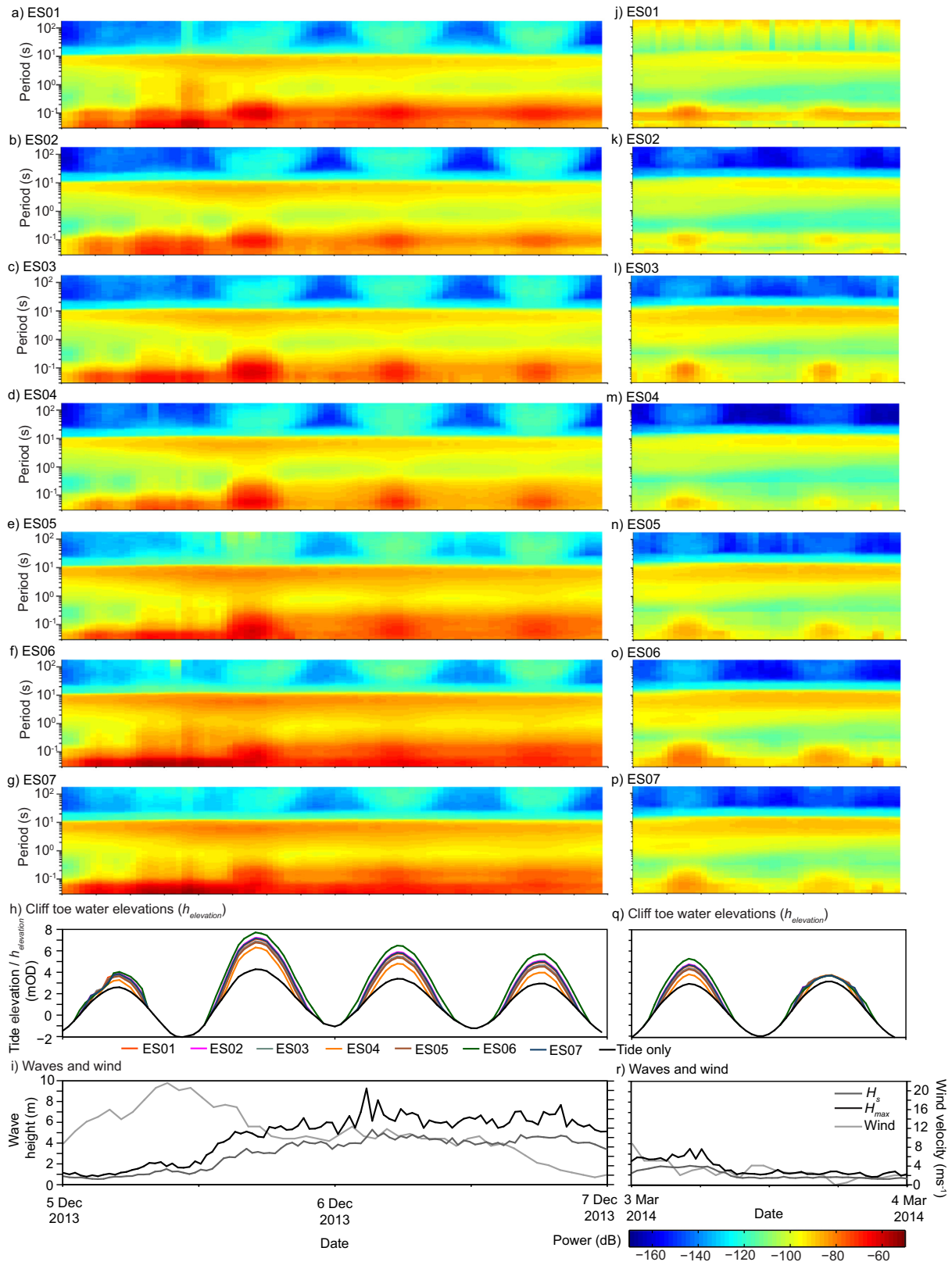


Fig. 5. Time series of spring tides during a–i) (first column) a storm occurring on 05–06/12/13; and j–r) (second column) less energetic conditions on 03/03/14. a–g & j–p) Spectrograms of the power spectral density across the seven seismometers (dB calculated as $10 \log_{10}((m s^{-1})^2/Hz)$) for the Z component, within the period/frequency range 0.03–180 s/33.3–0.0055 Hz, at a & j) ES01; b & k) ES02; c & l) ES03; d & m) ES04; e & n) ES05; f & o) ES06; g & p) ES07; h & q) concurrent tide and combined tide and wave elevation at the cliff toe ($h_{elevation}$) modelled for East Staithes; and i & r) significant wave height (H_s) and maximum wave height (H_{max}) recorded at the Whitby wave buoy, and wind velocity measured at Loftus (5 km from study site). Wave and tide data are courtesy of the North East Coastal Observatory (www.northeastcoastalobservatory.org.uk). Wind data are courtesy of the Met Office (2006).

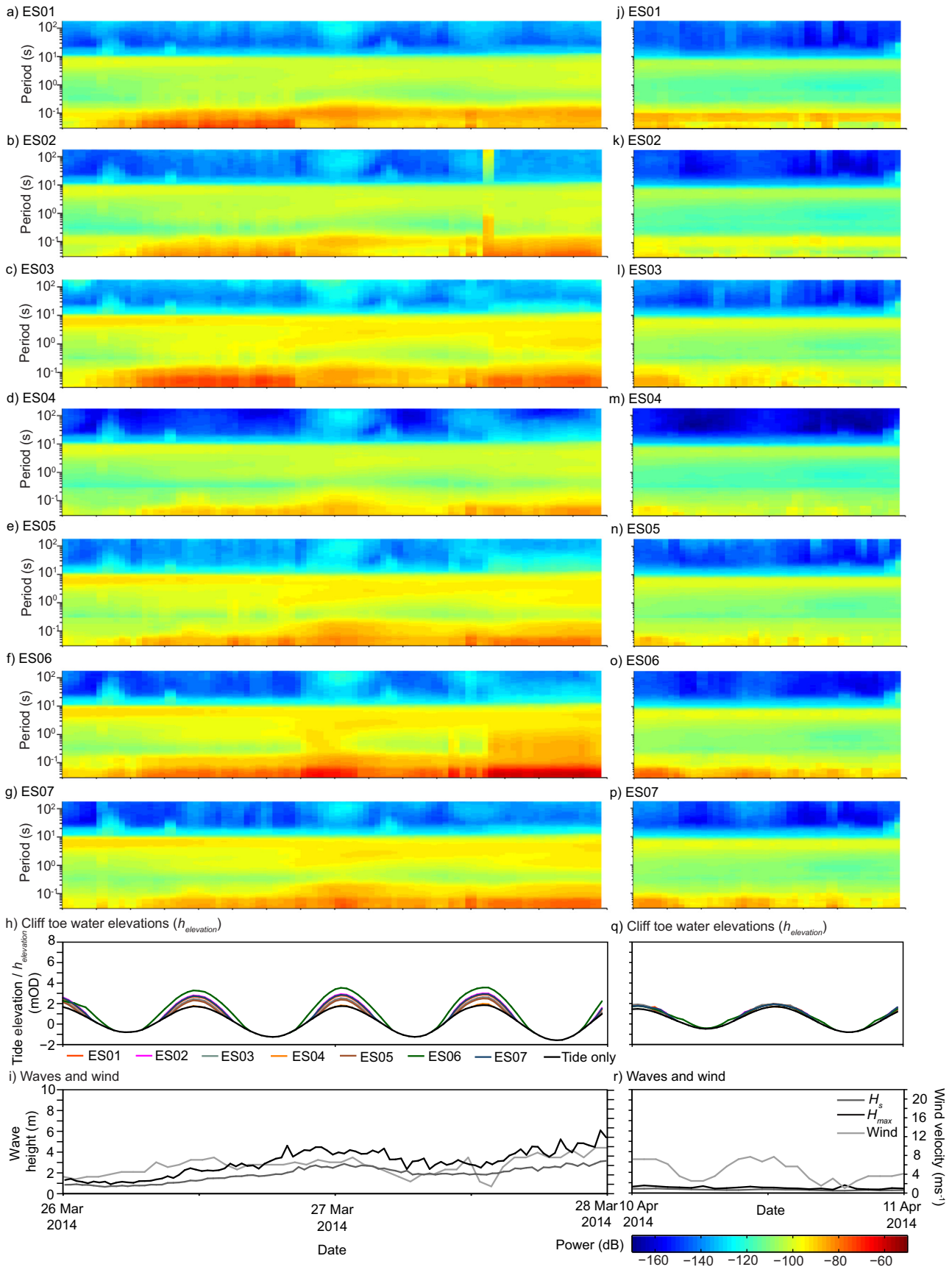


Fig. 6. Time series of neap tides during a–i) (first column) a storm occurring on 26–27/03/14; and j–r) (second column) less energetic conditions on 10/04/14. a–g & j–p) Spectrograms of the power spectral density across the seven seismometers (dB calculated as $10 \log_{10}((\text{m s}^{-1})^2/\text{Hz})$) for the Z component, within the period/frequency range 0.03–180 s/33.3–0.0055 Hz, at a & j) ES01; b & k) ES02; c & l) ES03; d & m) ES04; e & n) ES05; f & o) ES06; g & p) ES07; h & q) concurrent tide and combined tide and wave elevation at the cliff toe ($h_{elevation}$) modelled for East Staithes; and i & r) significant wave height (H_s) and maximum wave height (H_{max}) recorded at the Whitby wave buoy, and wind velocity measured at Loftus (5 km from study site). Wave and tide data are courtesy of the North East Coastal Observatory (www.northeastcoastalobservatory.org.uk). Wind data are courtesy of the Met Office (2006).

power across the marine-generated seismic signals. The HT signals are less clearly defined and lower power than both spring tide examples (Fig. 5) (e.g. -20 dB lower at ES06).

During low wave energy neap tides ($H_s = 0.32$ m, maximum wave height = 0.76 m) (Fig. 6j–r) there are no HT or LP ground motion signals. In the absence of the HT seismic signals, it is evident there is also high frequency shaking generated by wind (WI), particularly when velocities exceed ~ 7 m s $^{-1}$ at frequencies ≥ 10 Hz/ ≤ 0.1 s (Fig. 6r). The WI signal overlaps with the higher frequencies of the HT signal, however the WI signal is only generated during above-average wind velocities, and the spring tide examples (Fig. 5) demonstrate that the HT signal dominates the 3.3–33.3 Hz band. The difference in ground motion signals between the sites demonstrates that these signals are generated locally to each seismometer and that the sea conditions generating them vary across distances of < 79 m (the shortest distances between neighbouring seismometers).

4.2. Observed alongshore distribution of HT ground motion energy

The remainder of the analysis focuses on the HT ground motion signals to examine alongshore differences in wave-cliff impacts. The eastern headland in our study site, ES06, experiences the greatest HT ground motion energy in all metrics presented (Fig. 7): *Total* (4.22×10^{14} ($\mu\text{m s}^{-1}$) 2) (Fig. 7a); *Max_h* (117×10^3 ($\mu\text{m s}^{-1}$) 2)

(Fig. 7b) and 99th percentile of the *Max_h* (10.7×10^3 ($\mu\text{m s}^{-1}$) 2) (Fig. 7c).

ES07 has the second highest value of *Total* (2.67×10^{14} ($\mu\text{m s}^{-1}$) 2), just over half that at ES06 (Fig. 7a). The *Max_h* at ES07 is the lowest (3.1×10^3 ($\mu\text{m s}^{-1}$) 2) (Fig. 7b), indicating it is average wave conditions here that are more energetic relative to sites ES01–ES05, rather than the extreme events.

Whilst ES05 has a high relative *Max_h* value (104.8×10^3 ($\mu\text{m s}^{-1}$) 2) (Fig. 7b), the 99th percentile (3.2×10^3 ($\mu\text{m s}^{-1}$) 2) (Fig. 7c) indicates an outlier, the *Total* (Fig. 7a) is the third lowest, indicating it is actually a relatively low HT ground motion energy site. Site ES04 which lies at the centre of the bay has the lowest of all the measures of HT ground motion energy, with *Total* = 0.21×10^{14} ($\mu\text{m s}^{-1}$) 2 (Fig. 7a) 5% of that received at ES06. ES02 is also a relatively low-energy site, with the second lowest measures of HT ground motion energy (excluding *Max_h*) and *Total* = 0.46×10^{14} ($\mu\text{m s}^{-1}$) 2 , 12% of that at ES06 (Fig. 7a).

ES01, the western headland, has the largest *Max_h* HT ground motion energy (118×10^3 ($\mu\text{m s}^{-1}$) 2) (Fig. 7b), but the 99th percentile suggests this is, again, an outlier (5.8×10^3 ($\mu\text{m s}^{-1}$) 2) (Fig. 7c). The *Total* HT ground motion energy (1.95×10^{14} ($\mu\text{m s}^{-1}$) 2) is similar to that at ES03 (2.15×10^{14} ($\mu\text{m s}^{-1}$) 2) (Fig. 7a), which lies at the centre of the bay.

4.3. Controls of the observed alongshore variability in HT ground motion energy

The observed variability in microseismic ground motions implies that conditions that determine wave characteristics and energy delivery to the cliff toe vary between the seven positions monitored. The marine controls on signal variability are tested by examining the effects of both marine and foreshore variables. We consider cliff toe elevation, foreshore characteristics, tide and wave heights, and examine the effects of these on the ground motion signals recorded by the seven instruments.

Cliff toe elevation varies over 2.02 m between sites and is a key control of energy transfer to the cliffs (Fig. 8). ES06 experiences inundation over the greatest elevation range (R_{ind} , 8.2 m) and has the lowest cliff toe elevation (-0.62 m OD), a steep, narrow and smooth foreshore, conducive in form to ramping waves up-cliff (Fig. 8k). The greatest HT ground motion energy over the monitoring period (Figs. 7, 8l) is observed here. ES04 has the highest cliff toe elevation (1.4 m OD) and the most constricted range in inundation ($R_{ind} = 4.7$ m) (Fig. 8g), with lower tide water depths and thus wave heights. This instrument records the lowest HT energy (Figs. 7, 8h), indicating that significant wave energy dissipation occurs before waves reach the cliff toe at this location. Where foreshore topography enables waves to break closer to or at the cliff, more wave energy is transferred into cliff as HT ground motion.

The vertical distribution of *Total*, derived from $h_{elevation}$, varies between sites but again shows no systematic alongshore pattern that mirrors the coastal planform (Fig. 8). The foreshore profiles show that not only cliff toe elevation but also foreshore topography and width vary considerably between the seven sites (Figs. 2, 8). Peaks in *Total* (Fig. 8b, d, f, h, j, l, n) typically coincide with water levels at elevations most frequently inundated by $h_{elevation}$, or the zone just above (ES01–3, ES06–7), and broadly reflect the vertical inundation duration below 5 m OD (Fig. 8a, c, e, g, i, k, m). At all sites there is also an increase in *Total* when $h_{elevation}$ inundation is at its maximum in the largest albeit rarest storms. At sites ES02, ES04 and ES05, this is when the highest *Total* occurs (Fig. 8). ES02, ES04 and ES05 are the lowest HT ground motion energy sites suggesting that when the water level is at the more frequently inundated elevations of the cliff face, most incident wave energy is dissipated across the foreshore before reaching the cliff toe and that only during the largest storm events can significant energy be transferred to the cliff at these sites.

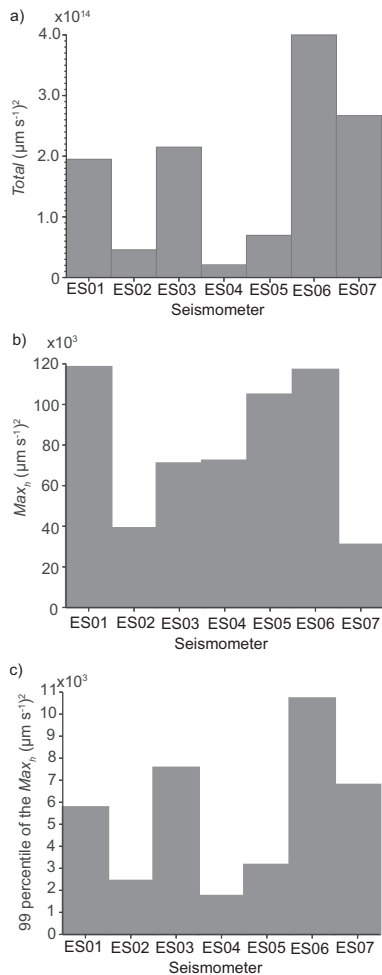


Fig. 7. Various statistics of HT ground motion energy ($(\mu\text{m s}^{-1})^2$) for each of the seven instruments over the monitoring period 29/11/2013 to 20/07/2014: a) total HT ground motion energy over the monitoring period (*Total*); b) hourly maximum (*Max_h*); c) 99th percentile of the *Max_h*.

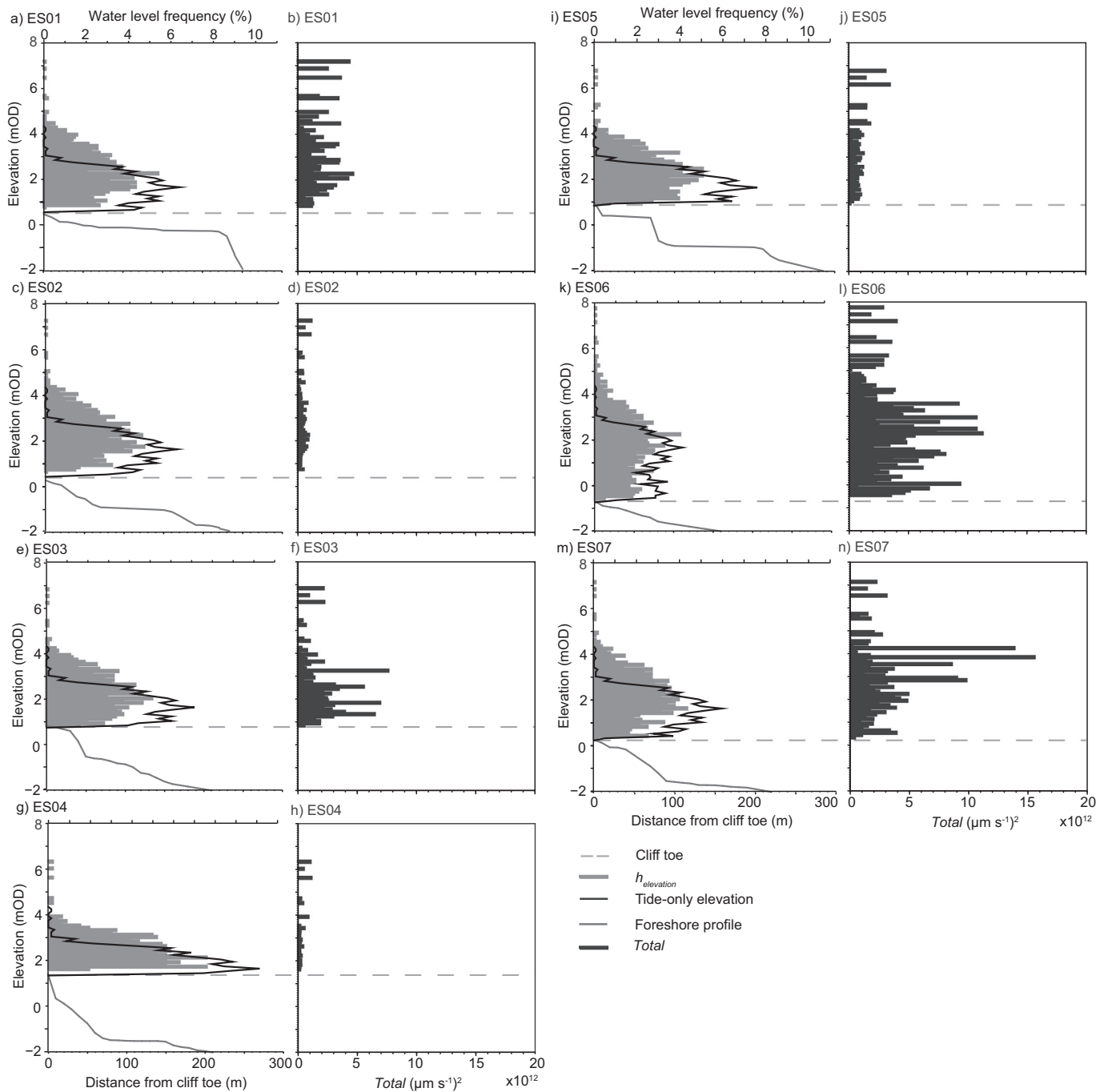


Fig. 8. Distributions of water level inundation frequency and total HT ground motion energy over the monitoring period (*Total*) up the cliff profile within the inundation zone during the monitoring period 29/11/2013–20/07/2014 for each of the seismometer locations: a & b) ES01; c & d) ES02; e & f) ES03; g & h) ES04; i & j) ES05; k & l) ES06; m & n) ES07. Inundation frequency (percentage) of tide-only (black line) and combined tide and wave elevation at the cliff toe ($h_{elevation}$) (grey bars) for 0.1 m bins of cliff elevation (a, c, e, g, i, k, m). The foreshore profile exposed at low spring tide is shown by the grey line. *Total* (black bars, Z component, 3–33 Hz) per 0.1 m elevation bin of $h_{elevation}$ inundation (b, d, f, h, j, l, n). The dashed grey line shows the elevation of the cliff toe.

At the sites which experience more energetic HT ground motions (ES06, ES07, ES03 and ES01) the vertical distribution of *Total* suggests that significant wave energy is transferred to the cliff throughout the tidal inundation cycle. Therefore, less wave energy is dissipated across the foreshore in front of the cliff in these locations. At these sites, the peak *Total* occurs at different elevations, likely representing the varying foreshore characteristics, and the resulting differences in shoaling of the incident wave field. As foreshore geometry varies in a non-systematic manner between adjacent sites, it is clearly a key control on the transfer of wave energy, influencing cliff microseismic excitation.

To examine the effect of cliff characteristics on the HT ground motion signal recorded at each seismometer, such as signal attenuation or amplification, and to determine the relative influence of these on *Total* compared to foreshore characteristics, metrics describing cliff and foreshore topography were correlated with *Total* (Fig. 9). Those that derived statistically-significant relationships (p -value ≥ 0.05) with *Total* are presented in Fig. 9.

Cliff toe elevation (Fig. 9a), the number of foreshore steps (Fig. 9b), and foreshore elevation change (Fig. 9c), all have a negative linear relationship with *Total* ($r^2 \geq 0.67$). The linear distance between the

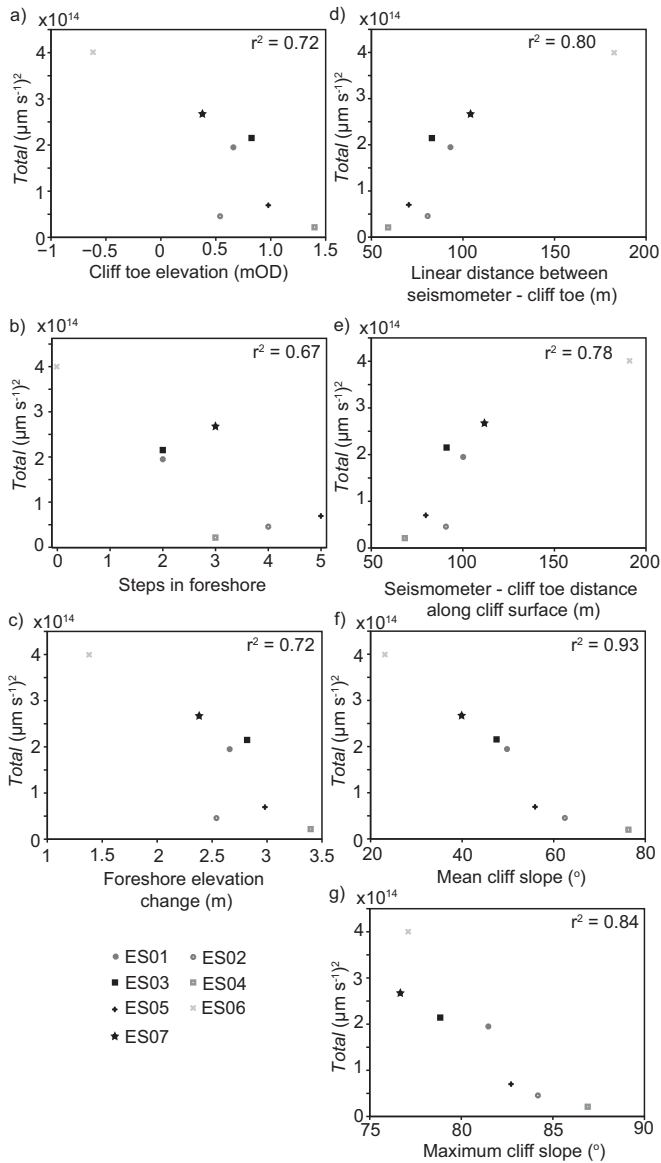


Fig. 9. Relationships between total HT ground motion energy over the monitoring period (*Total*) and foreshore and cliff characteristics: a) cliff toe elevation; b) number of steps in foreshore; c) foreshore elevation change; d) linear distance between seismometer-cliff toe; e) seismometer-cliff toe distance along cliff surface; f) mean cliff slope; and g) maximum cliff slope. Statistically significant relationships are presented (at p -value ≥ 0.05). Foreshore width and cliff height were also regressed against *Total* however were not statistically significant.

seismometer and the cliff toe, and the distance along the cliff surface, demonstrate positive linear relationships with *Total* ($r^2 = 0.80$ and 0.78 respectively, Figs. 9d, e), whilst the mean and maximum cliff slope have negative linear relationships ($r^2 = 0.93$ and 0.84 , respectively, Figs. 9f, g). The relationship between the seismic signal amplitude and both cliff slope and distance are the inverse of what would be expected if local cliff topography dominate the HT seismic signal amplitude (e.g. Ashford et al., 1997; Messaoudi et al., 2012). These results demonstrate that the relative amplitude of the HT ground motion signal alongshore is, on the whole, not determined by the effects of local cliff topography. Instead, the HT signal recorded is dominated by the microseismicity resulting from the interaction of the sea and the cliff toe, which in turn reflects the local variability in the foreshore characteristics (Fig. 9). This demonstrates that using the current seismometer array/set-up at this site, the HT ground motion signal provides a

valuable representation of marine conditions at the cliff toe local to the seismometer and enables alongshore comparison of HT signal amplitudes.

At all seven sites there is an apparent threshold of the combined tide and wave height above the cliff toe (h_{height} , m) at 2 m, above which there is an absence of smaller HT ground motion energy events and *Total_h* energy increases with h_{height} (Fig. 10). Despite the scatter in the data, on average we observe an order of magnitude increase in *Total_h* between h_{height} of 5 m and 7 m, increasing from $10 \times 10^{11} (\mu\text{m s}^{-1})^2$ to $10 \times 10^{12} (\mu\text{m s}^{-1})^2$. A similar behaviour above 2 m at all sites may suggest that water depths during the large storm events are deep enough that the local foreshore effects on wave shoaling are effectively overwritten, whereby a more uniform microseismic response is observed at all instruments.

5. Discussion

5.1. Overview of findings

We find HT ground motions reflect variations in foreshore topography and mirror the resulting variability in wave energy dissipation. We show distinct differences between the microseismic excitation of cliffs within bays and headlands. The observed microseismic ground motion is shown to encompass the complexity of nearshore wave climate, including refraction, foreshore and cliff toe characteristics, into a single measure, providing a relative measure of energy delivery to the cliffs.

5.2. The influence of foreshore morphology on HT ground motion energy

The alongshore distribution of HT microseismic energy is highly variable, with no pattern that obviously maps onto the bay-headland planform coastline geometry. Our results demonstrate the importance of the foreshore modification of waves in driving energy transfer to the cliff, which potentially then maps onto the resultant erosion response. Local alterations in water depth and foreshore topography play a key role in the alongshore distribution of wave energy that is available to generate cliff HT ground motions, and over-rides that of macroscale planform coastline geometry. Importantly the results show that these foreshore characteristics vary significantly over only short distances, here ca. 100 m. The exact position of a seismic monitoring station along a coast therefore holds a considerable influence on the nature of the HT ground motion signals that will be observed.

Cliff toe and foreshore elevation relative to the tidal range determines water depths and thus wave heights at the cliff and locations of wave breaking. The different elevations of the cliff toe across the monitored 1 km coastline examined here, relative to the macrotidal range (6 m), result in significant variability in high tide water depths (modelled maximum of 2.88–4.9 m above the cliff toe) and thus wave heights (modelled maximum wave heights of 2.03–3.44 m). These observations match those of recent studies that have used transects of pressure sensors to measure the cross-shore distribution of wave energy, and the corresponding wave spectra, on rock foreshores. Both are dependent on the foreshore morphology and cliff toe elevation relative to the tidal range (Ogawa et al., 2011, 2016; Poate et al., 2016; Stephenson et al., 2017). At sites with large macrotidal ranges (i.e. >7 m) during high tides and average wave conditions, pressure sensor data have shown the wave breakpoint to move landwards across the foreshore as tide levels rise (Poate et al., 2016; Stephenson et al., 2017) and increased corresponding wave energy density cross-shore (Stephenson et al., 2017). This effect can be seen at ES06 where the low cliff toe elevation and resulting deeper waters enable waves to break closer to/at the cliff as compared to at the other instrument locations (Fig. 2). In contrast the wide extent of high elevation foreshore at ES01, and resulting shallow water depths, means that waves break further away from the cliff than at the other sites (Fig. 2).

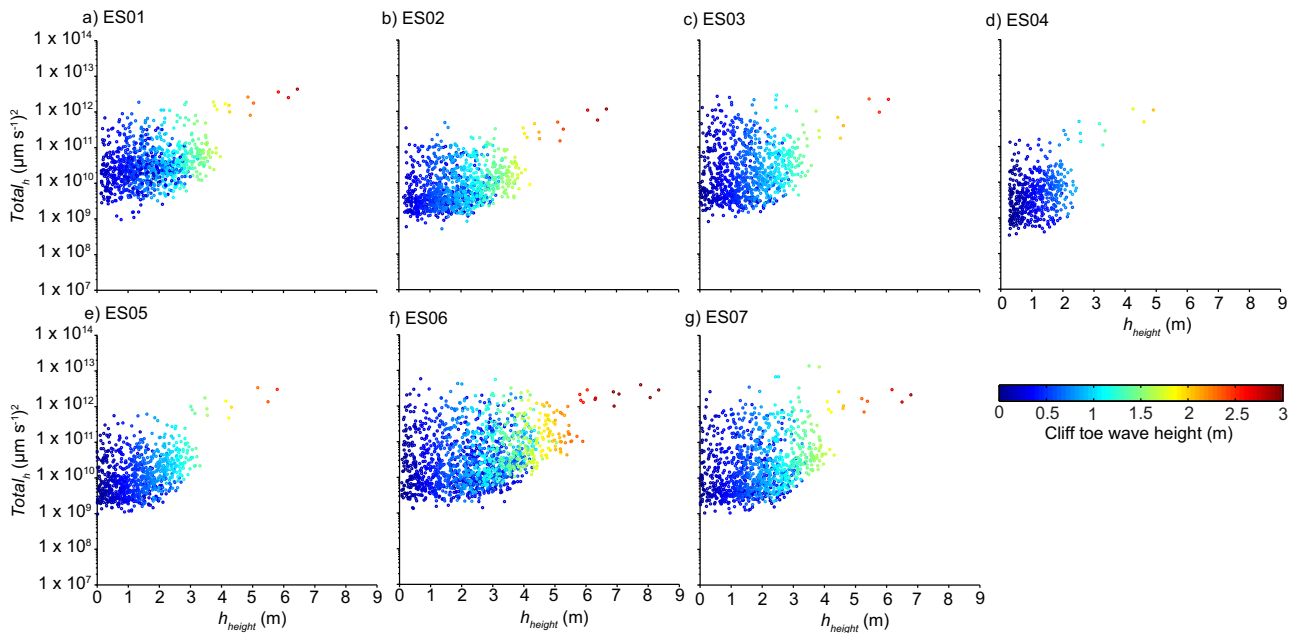


Fig. 10. Scatter plots of the relationship between hourly total HT ground motion energy ($Total_h$) and combined tide and wave height above the cliff toe (h_{height}) at the seven sites: a) ES01; b) ES02; c) ES03; d) ES04; e) ES05; f) ES06; g) ES07. Colour corresponds to modelled cliff toe wave height (m).

In a study of six microtidal platforms, [Ogawa et al. \(2016\)](#) found platform width and elevation to be dominant controls on wave energy reaching the cliff toe. More narrow and lower elevation platforms enable greater gravity wave energy to propagate across the platform due to greater water depths ([Ogawa et al., 2016](#)), which matches our observations where the greatest HT ground motion energy occurs at ES06. At higher elevation and wider microtidal platforms, greater gravity wave energy is dissipated across the platform and the ratio of infragravity to gravity energy increases towards the cliff due to the shallow water depths ([Beetham and Kench, 2011](#); [Ogawa et al., 2016](#)). However, at East Staithes, foreshore width did not derive a statistically significant relationship with HT ground motion energy observed at the cliff. This may be due to the complex foreshore topography, the presence of multiple steps, and the variability in between the seven instrument locations. Using pressure sensors across a ~300 m-wide macrotidal platform (11 m range), [Stephenson et al. \(2017\)](#) observed that high tide water depths enabled waves <2 m to travel unbroken across the platform, which only begin to break near the cliff toe, producing a narrow surf zone at the inner foreshore. At microtidal sites [Marshall and Stephenson \(2011\)](#) also found foreshore width to have a lesser influence on wave energy dissipation across the foreshore than foreshore gradient and water depths.

The relative importance of foreshore gradient is determined by elevation relative to the tidal range, in addition to the tidal range itself. The importance of gradient and width may thus change throughout the tidal cycle ([Ogawa et al., 2016](#)), and hence here between sites. The role of foreshore gradient is also complicated by the variability cross-shore, for example, by the presence of steps. This is confounded by the common simplification to use one value for a whole site, which may not be representative of the whole platform width, as would be the case at East Staithes. In this study, sites of low foreshore roughness (here measured as the number of steps, given the minimal boulder coverage on the foreshore on this section of coast) experience lower cross-shore wave energy dissipation relative to the other sites, also observed at other macrotidal rock foreshores by [Poate et al. \(2016\)](#).

Differences in MS and LP signal power between sites demonstrates the effect of the varied foreshore morphology on wave energy dissipation. Higher MS and LP signal power at sites indicates the foreshore is

conductive for propagating higher amounts of infragravity and gravity wave energy across the foreshore. The differences in HT total energy between sites, which exhibit similar MS/LP ground motion signals, indicate that foreshore characteristics near the cliff toe play a key role in dissipating wave energy and determining whether waves have already broken at the instant when they impact against the cliff toe.

Our results show that HT ground motion energy across the seven sites becomes more similar in character during an extreme storm, as compared to low energy, or indeed average, conditions ([Figs. 5, 6](#)). The difference in water depths and modelled wave heights at the toe of the seven sites, however, suggests that the levels of HT ground motion energy recorded at the seven sites during the storm do not represent similarities in wave heights, but instead may indicate similarities in wave-cliff face interaction, such as a more uniform pattern of waves breaking onto the cliff toe. At Scots Bay in the Bay of Fundy, another macrotidal site, during storm conditions [Trenhaile and Kanyaya \(2007\)](#) observed narrowing surf zones, lower levels of wave attenuation and more energetic types of breaking waves (plunging breakers) in the upper foreshore during high tides. This was compared to the lower platform during lower tide levels and was attributed to greater water depths and higher platform gradients at the upper foreshore. Our results may suggest that similar cross-shore shifts in wave characteristics occur at our site during large storms, and that water depths are sufficiently deep that the effects of the variable foreshore characteristics between sites are negated, and therefore so too are the differences in wave breaking across the foreshore. We identify a threshold depth of ca. 2 m above the cliff toe ([Fig. 10](#)), above which we suggest conditions assimilate across the seven sites, as less wave energy dissipation occurs and more waves break directly against the cliff toe to generate HT cliff shaking.

5.3. The influence of coastline geometry on HT ground motion energy

Using HT ground motion energy as a proxy for wave energy transfer to the cliff toe, we demonstrate that at this hard rock, low-sediment coast, the relative energy observed at different positions alongshore is determined more by foreshore characteristics than the macro-scale coastline planform morphology. Coastline planform may rather be more influential in determining the difference in HT ground motion

energy at the two headlands. Carter et al. (1990) and Limber et al. (2014) observed from field studies and modelling that energy observed at headlands is determined by the degree of coastline projection seaward, and thus exposure to incoming waves. At this study site, the ES06 headland protrudes slightly further from the bay as compared to the ES01 headland, and to the east of ES06 and ES07 the coastline drops away to the south (Fig. 1). Whilst both headlands are exposed to the dominant north-easterly waves, the greater projection seaward, and the southerly orientation of the coast to the east of the headland ES06 (Fig. 1), means that this site is exposed to a greater range of wave directions than ES01.

In Limber et al.'s (2014) numerical wave transformation model, headlands that protrude further induce greater wave refraction and convergence, and thus receive greater wave energy via wave-rock impacts. Whilst the greatest energy occurs at headland ES06 in our study, the lower foreshore elevation and deeper waters around the headland mean that during the dominant NE wave directions there is actually little wave refraction around the headland itself (Fig. 1d), and rather greater energy is due to the higher water depths around the headland. The difference in foreshore characteristics at ES06 and ES01 may in part be due to their relative exposure to the incident wave field and the resulting erosion of the foreshore. The coastline characteristics also likely explain why ES07, on the eastern flank of the ES06 headland, has the second highest energy total, and supports Komar's (1985) suggestion that greatest energy would be expected at the headland point (ES06). The geometry of the two headlands is also different, with ES01 being wider alongshore, shorter cross-shore and more rounded in planform. ES06 is narrower, longer and similar to the 'needle-like' headlands characterised by Komar (1985). Interestingly, the relative energy and planform morphologies is counter to that observed by Carter et al. (1990) in Nova Scotia, who found stubby, rounded headlands to form in more exposed, higher energy positions.

5.4. Cliff ground motions as proxies of cliff toe wave energy

This study builds on the previous body of work using single cliff-top seismometers that have demonstrated high frequency cliff shaking to be a valuable proxy of relative wave energy transfer to the cliff toe (Vann Jones et al., 2015; Young et al., 2016). We have demonstrated that the magnitude of cliff toe wave impact generated ground motions varies significantly alongshore and even over short distances (here ~100 m).

The wave-cliff impact signal (HT) frequency range varies between this and other microseismic studies globally (e.g. >0.3 Hz (Young et al., 2011), 7–20 Hz (Dickson and Pentney, 2012), 1.1–50 Hz (Norman et al., 2013; Vann Jones et al., 2015), 20–45 Hz (Young et al., 2016)). Young et al. (2013) observed a range of bands between 2 and 40 Hz across a variety of soft and hard rock cliffs globally. The range of frequency bands observed indicates differences in site response to, and local effects on, wave-cliff impacts. Young et al. (2013) attribute the variability in site response to combinations of tide elevation, wave energy, site morphology and geology and local signal decay. Rock foreshores clearly complicate wave-cliff impact microseismic signals and result in significant variations between even contiguous sites because of the feedbacks between the foreshore and wave breaking and attenuation. Key to this is the elevation relative to the tidal range, and thus where waves break relative to the cliff toe. For example, at a meso-tidal site of high foreshore elevation relative to the high tide level, Dickson and Pentney (2012) observed the wave-cliff impact signal to be generated during low tides as waves broke at the steep seaward edge of the foreshore and shallow depths across the platform dissipated wave energy before reaching the cliff toe.

The exact area of signal generation at the cliff toe is unknown and further work is required to examine concurrently monitored cliff toe and foreshore wave conditions and cliff-top ground motions, to improve our understanding of cliff toe waves. However, the differences in HT signals between sites in this study demonstrate that the HT signals are generated

by cliff-wave impacts local to each seismometer, whereby small distances along coast can result in very different behaviours observed.

Some of the variation observed in ground motion energy across the sites must be considered a function of local site and instrument effects, which influence to some degree signal attenuation and amplification, including instrument-ground coupling, cliff material and structure (Lowrie, 1997; Stein and Wysession, 2003), topography (Ashford et al., 1997), and moisture content (Mavko et al., 1998). However, identifying, testing and quantifying these effects on the signals and calibrating signals recorded at each site remains challenging. In simple analysis of the relationship between HT signal energy and cliff morphology, such as the slope and distance from seismometer-cliff toe, we found the HT signal to be dominated by cliff toe wave conditions, which are of a magnitude that dominates any influence of instrument position or highly local site effects in our array (e.g. Ashford et al., 1997; Messaoudi et al., 2012). Inevitably, with more structural, geological or topographic variability between sites, such effects must at some point become significant.

HT ground motion signals have been found to have the strongest correlations with observed cliff face erosion, as compared to microseism (MS) and long period (LP) frequency bands (Vann Jones et al., 2015). As a result, we argue that our findings may have important implications for how wave-driven cliff erosion is distributed alongshore and more work is required to examine this further.

6. Conclusions

High frequency cliff motions (HT) generated by wave-cliff impacts provide a valuable proxy measure of the relative wave energy transfer along a coast at the cliff toe. Using an array of seven cliff-top seismometers placed at ca. 100 m intervals along a 1 km stretch of coastline, we quantified the alongshore distribution of relative wave energy transfer. There is no systematic alongshore pattern in microseismic HT ground motion energy recorded by the seismometers during the monitoring period around the bay and headlands study site. The greatest HT ground motion energy occurs at a headland and the lowest at the centre of the bay (5% of the headland). However, there is an order of magnitude difference in total HT ground motion energy between some neighbouring sites within the bay, and the two headlands experience very different relative HT energies (energy at the eastern headland is 49% of the western headland). We suggest that the significant variations in foreshore characteristics observed here are responsible for the alongshore variations in the (modelled) cliff toe water elevations and corresponding HT ground shaking energy observed. Importantly, the effect of the foreshore on wave energy dissipation overrides the influence of macroscale coastal planform geometry. We suggest that the alongshore variability in wave energy focussing over short distances controlled by local variability in foreshore characteristics that we observe will inevitably hold important implications for the distribution of resulting cliff erosion, and more work is required to examine this further.

Acknowledgements

The authors gratefully acknowledge the funding for this research provided by ICL (Fertilizers) Ltd. UK. The seismic equipment was provided by NERC's SEIS-UK (loan number 985) and the authors are grateful for support provided by Victoria Lane and David Hawthorn. Wave and tide data are courtesy of the North East Coastal Observatory (www.northeastcoastalobservatory.org.uk). Wind data are courtesy of the Met Office (2006). Many thanks to the National Trust and David Barker for permission to use and regularly access the study site, and to Samantha Waugh and David Hodgson for help with fieldwork. Thanks also to Jess Benjamin and Zuzanna Swirad for assistance in producing Fig. 1. We thank A Young and M Dickson for their constructive and insightful review of our manuscript.

References

- Adams, P.N., Storlazzi, C.D., Anderson, R.S., 2005. Nearshore wave-induced cyclical flexing of sea cliffs. *J. Geophys. Res. F: Earth Surf.* 110, F02002. <https://doi.org/10.1029/2004JF000217>.
- Ashford, S.A., Sitar, N., Lysmer, J., Deng, N., 1997. Topographic effects on the seismic response of steep slopes. *Bull. Seismol. Soc. Am.* 87 (3), 701–709.
- Battjes, J.A., Stive, M.J.F., 1985. Calibration and verification of a dissipation model for random breaking waves. *J. Geophys. Res. Oceans* 90 (NC5), 9159–9167. <https://doi.org/10.1029/JC090iC05p09159>.
- Beetham, E.P., Kench, P.S., 2011. Field observations of infragravity waves and their behaviour on rock shore platforms. *Earth Surf. Process. Landf.* 36 (14), 1872–1888. <https://doi.org/10.1002/esp.2208>.
- Bormann, P. (Ed.), 2009. *New Manual of Seismological Observatory Practise (NMSOP-1)*. IASPEI, GFZ German Research Centre for Geosciences https://doi.org/10.2312/GFZ.NMSOP_r1_ch1.
- Bowman, D., Guillen, J., Lopez, L., Pellegrino, V., 2009. Planview geometry and morphological characteristics of pocket beaches on the Catalan coast (Spain). *Geomorphology* 108 (3–4), 191–199. <https://doi.org/10.1016/j.geomorph.2009.01.005>.
- Bray, M.J., Hooke, J.M., 1997. Prediction of soft-cliff retreat with accelerating sea-level rise. *J. Coast. Res.* 13, 453–467.
- Carter, R.W.G., Jennings, S.C., Orford, J.D., 1990. Headland erosion by waves. *J. Coast. Res.* 6 (3), 517–529.
- Dickson, M.E., Pentney, R., 2012. Micro-seismic measurements of cliff motion under wave impact and implications for the development of near-horizontal shore platforms. *Geomorphology* 151–152, 27–38. <https://doi.org/10.1016/j.geomorph.2012.01.006>.
- Dickson, M.E., Walkden, M.J.A., Hall, J.W., 2007. Systemic impacts of climate change on an eroding coastal region over the twenty-first century. *Clim. Chang.* 84 (2), 141–166. <https://doi.org/10.1007/s10584-006-9200-9>.
- Earlie, C.S., Young, A.P., Masselink, G., Russell, P.E., 2015. Coastal cliff ground motions and response to extreme storm waves. *Geophys. Res. Lett.* 42 (3), 847–854. <https://doi.org/10.1002/2014gl062534>.
- Friedrich, A., Kruger, F., Klinge, K., 1998. Ocean-generated microseismic noise located with the Grafenberg array. *J. Seismol.* 2, 47–64.
- Hapke, C.J., Reid, D., Richmond, B., 2009. Rates and trends of coastal change in California and the regional behavior of the beach and cliff system. *J. Coast. Res.* 25 (3), 603–615. <https://doi.org/10.2112/08-1006.1>.
- Hedlin, M.A.H., Orcutt, J.A., 1989. A comparative study of island, seafloor, and seabed ambient noise-levels. *Bull. Seismol. Soc. Am.* 79, 172–179.
- Klein, A.H.D., de Menezes, J.T., 2001. Beach morphodynamics and profile sequence for a Headland Bay Coast. *J. Coast. Res.* 17 (4), 812–835.
- Komar, P.D., 1985. Computer models of shoreline configuration: headland erosion and the graded beach revisited. In: Woldenberg, M.J. (Ed.), *Models in Geomorphology*. Allen and Unwin, London, pp. 139–154.
- Komar, P.D., 1997. *Beach Processes and Sedimentation*. Prentice Hall, Upper Saddle River, N.J.
- Limber, P.W., Murray, A.B., 2011. Beach and sea-cliff dynamics as a driver of long-term rocky coastline evolution and stability. *Geology* 39 (12), 1147–1150. <https://doi.org/10.1130/G32315.1>.
- Limber, P.W., Murray, A.B., Adams, P.N., Goldstein, E.B., 2014. Unraveling the dynamics that scale cross-shore headland relief on rocky coastlines: 1. Model development. *Journal of Geophysical Research-Earth Surface* 119 (4), 854–873. <https://doi.org/10.1002/2013jf002950>.
- Longuet-Higgins, M.S., 1950. A theory of the origin of microseisms. *Philos. Trans. R. Soc. Lond. A* 243, 1–35.
- Lowrie, W., 1997. *Fundamentals of Geophysics*. Cambridge University Press, Cambridge; New York, NY, USA.
- Marshall, R.J.E., Stephenson, W.J., 2011. The morphodynamics of shore platforms in a micro-tidal setting: Interactions between waves and morphology. *Mar. Geol.* 288 (1–4), 18–31. <https://doi.org/10.1016/j.margeo.2011.06.007>.
- Mavko, G., Mukerji, T., Dvorkin, J., 1998. *The Rock Physics Handbook: Tools for Seismic Analysis in Porous Media*. Cambridge University Press, Cambridge.
- Messaoudi, A., Laouami, N., Mezour, N., 2012. Topographic effects on the seismic responses of slopes. *Proceedings of the 15th World Conference on Earthquake Engineering*. Portugal, Lisbon.
- Met Office (2006): MIDAS: UK Hourly Weather Observation Data. NCAS British Atmospheric Data Centre, accessed 26/03/18. <http://catalogue.ceda.ac.uk/uuid/916ac4bbc46f7685ae9a5e10451bae7c>
- Murray, A.B., Ashton, A.D., 2013. Instability and finite-amplitude self-organization of large-scale coastline shapes. *Philos. Trans. R. Soc.* 371, 20120363. <https://doi.org/10.1098/rsta.2012.0363>.
- Norman, E.C., Rosser, N.J., Brain, M.J., Petley, D.N., Lim, M., 2013. Coastal cliff-top ground motions as proxies for environmental processes. *J. Geophys. Res. Oceans* 118 (12), 6807–6823. <https://doi.org/10.1002/2013jc008963>.
- Ogawa, H., Dickson, M.E., Kench, P.S., 2011. Wave transformation on a sub-horizontal shore platform, Tatapouri, North Island, New Zealand. *Cont. Shelf Res.* 31 (14), 1409–1419. <https://doi.org/10.1016/j.csr.2011.05.006>.
- Ogawa, H., Dickson, M.E., Kench, P.S., 2016. Generalised observations of wave characteristics on near-horizontal shore platforms: synthesis of six case studies from the North Island, New Zealand. *N. Z. Geogr.* 72 (2), 107–121. <https://doi.org/10.1111/nzg.12121>.
- Poate, T., Masselink, G., Austin, M., Dickson, M., Kench, P., 2016. Observation of wave transformation on macro-tidal rocky platforms. *J. Coast. Res.*, 602–606 <https://doi.org/10.2121/si75-121.1>.
- Sallenger, A.H., Krabill, W., Brock, J., Swift, R., Manizade, S., Stockdon, H., 2002. Sea-cliff erosion as a function of beach changes and extreme wave runup during the 1997–1998 El Niño. *Mar. Geol.* 187 (3–4), 279–297. [https://doi.org/10.1016/S0025-3227\(02\)00316-x](https://doi.org/10.1016/S0025-3227(02)00316-x).
- Stein, S., Wysession, M., 2003. *An Introduction to Seismology, Earthquakes, and Earth Structure*. Blackwell, Oxford.
- Stephenson, W.J., Kirk, R.M., 2000. Development of shore platforms on Kaikoura Peninsula, South Island, New Zealand – part one: the role of waves. *Geomorphology* 32 (1–2), 21–41. [https://doi.org/10.1016/S0169-555X\(99\)00061-6](https://doi.org/10.1016/S0169-555X(99)00061-6).
- Stephenson, W.J., Naylor, L.A., Smith, H., Chen, B., Brayne, R.P., 2017. Wave transformation across a macrotidal shore platform under low to moderate energy conditions. *Earth Surf. Process. Landf.* <https://doi.org/10.1002/esp.4245>.
- Sunamura, T., 1976. Feedback relationship in wave erosion of laboratory rocky coast. *J. Geol.* 84 (4), 427–437. <https://doi.org/10.1086/628209>.
- Sunamura, T., 1977. Relationship between wave-induced cliff erosion and erosive force of waves. *J. Geol.* 85 (5), 613–618. <https://doi.org/10.1086/628340>.
- Sunamura, T., 1982. A wave tank experiment on the erosional mechanism at a cliff base. *Earth Surf. Process. Landf.* 7 (4), 333–343. <https://doi.org/10.1002/esp.3290070405>.
- Sunamura, T., 1992. *Geomorphology of rocky coasts*. Coastal Morphology and Research. J. Wiley, Chichester; New York.
- Trenhaile, A.S., 1987. *The Geomorphology of Rock Coasts*. Oxford Research Studies in Geography. Clarendon Press, Oxford.
- Trenhaile, A.S., 2011. Predicting the response of hard and soft rock coasts to changes in sea level and wave height. *Clim. Chang.* 109, 599–615. <https://doi.org/10.1007/s10584-011-0035-7>.
- Trenhaile, A.S., Kanyaya, J.I., 2007. The role of wave erosion on sloping and horizontal shore platforms in macro- and mesotidal environments. *J. Coast. Res.* 23, 298–309. <https://doi.org/10.2112/04-0282.1>.
- Vann Jones, E.C., Rosser, N.J., Brain, M.J., Petley, D.N., 2015. Quantifying the environmental controls on erosion of a hard rock cliff. *Mar. Geol.* 363, 230–242. <https://doi.org/10.1016/j.margeo.2014.12.008>.
- Walkden, M.J.A., Hall, J.W., 2005. A predictive mesoscale model of the erosion and profile development of soft rock shores. *Coast. Eng.* 52 (6), 535–556. <https://doi.org/10.1016/j.coastaleng.2005.02.005>.
- Young, A.P., Adams, P.N., O'Reilly, W.C., Flick, R.E., Guza, R.T., 2011. Coastal cliff ground motions from local ocean swell and infragravity waves in southern California. *J. Geophys. Res. Oceans* 116, C09007. <https://doi.org/10.1029/2011jc007175>.
- Young, A.P., Guza, R.T., Adams, P.N., O'Reilly, W.C., Flick, R.E., 2012. Cross-shore decay of cliff top ground motions driven by local ocean swell and infragravity waves. *J. Geophys. Res. Oceans* 117. <https://doi.org/10.1029/2012jc007908>.
- Young, A.P., Guza, R.T., Dickson, M.E., O'Reilly, W.C., Flick, R.E., 2013. Ground motions on rocky, cliffed, and sandy shorelines generated by ocean waves. *J. Geophys. Res. Oceans* 118. <https://doi.org/10.1002/2013JC008883>.
- Young, A.P., Guza, R.T., O'Reilly, W.C., Burvint, O., Flick, R.E., 2016. Observations of coastal cliff base waves, sand levels, and cliff top shaking. *Earth Surf. Process. Landf.* 41 (11), 1564–1573. <https://doi.org/10.1002/esp.3928>.